JOURNAL OF MATERIALS SCIENCE 22 (1987) 1097–1107

Double torsion testing of high velocity crack resistance

P. S. LEEVERS, J. G. WILLIAMS
Department of Mechanical Engineering, Imperial College of Science and Technology, London SW7 2BX, UK

Field tests show that cracks can propagate steadily at more than 300 m sec^{-1} along gas-pressurized pipelines of normally ductile polyethylene, once initiated by impact. Although the determination of safe operating conditions demands a knowledge of the pipe material's resistance R to such high-velocity cracks, devising an appropriate small-scale test presents major problems. Instrumented drop-weight testing of double torsion specimens offers a promising solution: constant-velocity brittle crack propagation is observed and, since the static deformation mode remains admissible in the dynamic régime, a simple analysis is possible. From displacement data, this provided quite consistent results up to 200 m sec^{-1} crack velocity, whilst load measurements were more affected by transient torsional wave propagation. A simple dynamic analysis satisfying more boundary conditions supports the displacement-based quasi-static results, and offers to extend the method to higher crack velocities.

1. Introduction

A major factor in the design of plastic pipes has been the avoidance of cracking. In the past, the observation that slow crack growth can occur, usually after some initiation period, has motivated the selection of materials on the basis of crack resistance versus crack speed data, measured under what were judged to be particularly severe conditions. For polyethylene, for example, cracks are grown at 80° C in a dilute detergent solution [1]. This approach assumes that pipes are subjected to steady loading in service, but that overloading due to poor laying or ground movements would be resisted by the same mechanisms.

As in all design exercises, a single failure mode has been identified as the most critical, and criteria developed to avoid its occurrence. It is, of course, possible to envisage other events which could give rise to failure, and another which has been discussed recently as perhaps more critical is that of continuous rapid crack growth arising from impact on a pressurized pipe [2]. Self-sustaining crack propagation of this type has long been observed in steel pipes, and has also been reported in plastics [3]. An upper-bound analysis based on the worst possible set of circumstances has been used to assess this situation [4]. In a pipe of diameter D and wall thickness B under pressure p, the strain energy per unit length is

$$u_c = \left(\frac{\sigma^2}{2E}\right)\pi DB$$

where σ is the hoop stress $\sigma = (pD)/2B$. It is now assumed that all of this energy is available to create new surface area, and if R is the energy per unit plane area required to do this (a material property equivalent to G_c, the critical strain energy release rate), then that required per unit pipe length is RB. Equating these two quantities yields the result

$$ER = K_c^2 = \frac{\pi}{4}\frac{p^2D^3}{B^2} \quad (1)$$

For a given material of crack resistance R (or critical stress intensity factor K_c), we therefore have a limiting pressure, for any given pipe, below which the crack will not propagate, so the determination of R is of particular importance. British Gas [2] used an instrumented Charpy impact test to find K_c at initiation, and have checked the results by performing full-scale tests on pipes. The comparison proved inconclusive, since secondary variables such as test temperature appear to have a much larger effect than expected, but reassuring in that it proved difficult to make cracks grow for any distance. The issues are difficult to resolve in full-scale tests, which are limited in number by cost and time considerations.

Much interest has been generated by a suggestion of van Crombrugge [5] to use a smaller scale test in which a short length of pipe ($\simeq$ 1 m) is pressurized, and then a small crack is initiated at one end by an impact. Materials are then compared on the basis of how far through the sample the crack propagates. This is a much easier test than the full-scale version but, of course, lacks the effect of soil loading, etc.; more seriously, since the impact energy and pressure are fixed, it measures only the energy required to initiate a crack. Since materials with high impact initiation resistance leave less energy to drive subsequent propagation, good correlations have been reported [6] between van Crombrugge test data and performance in other impact initiation (e.g. Charpy) tests.

Indeed, most of these small-scale tests are limited to comparing materials in the crack initiation régime ($\dot{a} = 0$), whereas it is their resistance to cracks running at velocities of, say, $\dot{a} = 200$ to 300 m sec^{-1} which may be critical. In accidental impact damage, it must be assumed that there will be more than enough

0022–2461/87 $03.00 + .12 © *1987 Chapman and Hall Ltd.*

energy to initiate such a failure, and our concern should be to measure the material's resistance to crack propagation. The ideal solution is a small-scale laboratory test in which the crack is propagated at a controllable and uniform speed at which R (or K_{IC}) can be measured. Such tests present major problems; since their duration is necessarily short, transducer and recorder limitations make measurements difficult – though less so as technology advances. More profound are the problems of calculating the energy balance in a high-speed cracking process, in which inertial loads and kinetic energy exchanges may be very high. These problems are compounded for the polyethylenes used on gas pipes because they are, by design, extremely tough and resistant to crack initiation, and it is difficult to induce crack propagation at all.

All of these problems are, it appears, overcome by the use of the impact loaded double torsion (DT) test described here. Attempts to grow cracks in tension tests fail because high nett-section stresses induce ductile tearing, but the double torsion configuration gives rather low stresses. In addition, the grooving of the specimen which is necessary to control crack direction promotes brittle failure by suppressing surface plane-stress zones. It has been found that by cooling polyethylene specimens to 0° C in iced water (a reasonable simulation of the worst-case UK service environment), and impacting them at over $6\,\mathrm{m\,sec^{-1}}$, a crack could be propagated through the entire section ($\simeq 150\,\mathrm{mm}$) at velocities of up to $200\,\mathrm{m\,sec^{-1}}$. This method has long proved attractive for slow growth investigation because of its ability to control the crack velocity $\dot{a}$ with the displacement rate, and this feature is to some extent retained in the high speed régime. Finally, and most importantly, the simple static deformation system enables kinetic energy to be computed exactly for the "quasi-static" case, in which a constant rotation rate at the load point, and a constant crack speed (conditions followed during tests), are maintained in a specific relationship. This enables R (and hence K_c) to be computed as a function of $\dot{a}$, to provide the sought-for material assessment.

2. Analysis: quasi-static conditions

Crack resistance R can be calculated by computing strain (U_e) and kinetic (U_k) energy changes, and the external work done (E), during extension of a crack of length a and width B_c, and employing the energy balance

$$P_R = \frac{dE}{da} - \frac{dU_e}{da} - \frac{dU_k}{da} \qquad (2)$$

The crack resisting force P_R is simply RB_c for a straight-fronted crack, but for the highly curved DT crack front a correction is necessary [7] which we will neglect in the sequel to avoid obscuring other issues.

A quasi-static deformation model for the DT specimen is well established, and recent developments of it [8] help to explain some dynamic phenomena. Each half of the specimen behaves as a simple torsion beam for its entire length $(L' - L) < x < L'$ (Fig. 1). According to Saint-Venant torsion theory, any rectangular section BH undergoes only simple rotation ϕ and out-of-plane deflection $u = u(y, z, \partial\phi/\partial x)$, and transmits a torque

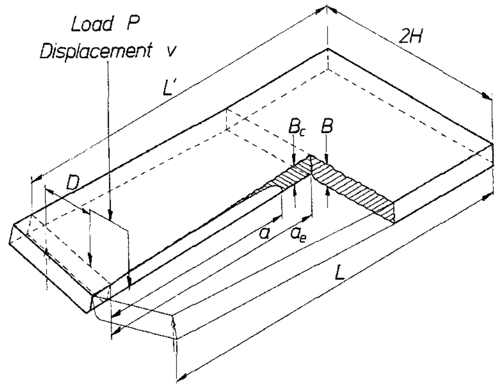

Figure 1 Double torsion (DT) specimen geometry.

$$T(x) = -\mu K \frac{\partial \phi}{\partial x} \qquad (3)$$

where the torsional rigidity is

$$\mu K = \mu Z H B^3 \qquad (4)$$

μ being the shear modulus and $Z(B/H)$ a function usefully approximated by

$$Z = \tfrac{1}{3} - 0.24\left(\frac{B}{H}\right) + 0.13\left(\frac{B}{H}\right)^2 \qquad (5)$$

In the static case, $\partial T/\partial x = 0$ in $0 < x < a$ so that $\phi(x)$ is linear. Each beam can be regarded as free up to the crack tip $x = a$, but subject to a restoring torque proportional to ϕ, and acting at the crack plane, in $a < x < L'$. A simple model [8] shows ϕ to be non-zero at $x = a$, but to extrapolate to zero at

$$a_e = a + \frac{2}{B_c}\left[\frac{6c}{\pi}\frac{1}{(1+\nu)} Z H B^3\right]^{1/2} \qquad (6)$$

(for sufficiently large $(L' - a)$). The factor c was estimated as 1.5 in earlier work, but re-analysis of the data, taking into account finite rotation effects [9] leads us to a revised estimate of 4. For most purposes, the displacement system is well described by

$$\left.\begin{aligned} \phi &= \theta\left(1 - \frac{x}{a_e}\right), \quad 0 < x < a_e \\ \phi &= 0 \qquad\qquad\quad\;\, , \quad x > a_e \end{aligned}\right\} \qquad (7)$$

where $\theta \equiv \phi(0)$, the imposed end rotation.

In the dynamic case, the torque $T(x)$ decays according to

$$\frac{\partial T}{\partial x} = \varrho I \frac{\partial^2 \phi}{\partial t^2} \qquad (8)$$

ϱ being the density and ϱI the polar mass moment of inertia

$$\varrho I = \tfrac{1}{12}\varrho B H (B^2 + H^2) \qquad (9)$$

Since from Equation 7 we have, noting that $\dot{a} = \dot{a}_e$ (dots denoting time derivatives),

$$\ddot{\phi} \equiv \frac{\partial^2 \phi}{\partial t^2} = \ddot{\theta}\left(1 - \frac{x}{a_e}\right) + 2\left(\dot{\theta} - \frac{\theta \dot{a}}{a_e}\right)\frac{\dot{a}}{a_e}\frac{x}{a_e} + \theta \frac{\ddot{a}}{a_e}\frac{x}{a_e} \qquad (10)$$

there is an additional non-dynamic ($\dot{\phi} = 0$ everywhere) solution at

$$\dot{a} = \frac{\dot{\theta} a_{\mathrm{e}}}{\theta} \equiv \dot{a}_{\mathrm{s}} \tag{11}$$

defining a constant steady-state crack velocity. Since $\phi' \equiv \partial\phi/\partial x = \theta/a_{\mathrm{e}}$ and $\dot{\phi} = \dot{\theta}$, the total strain and kinetic energies are then simply

$$U_{\mathrm{e}} = \int_0^{a_{\mathrm{e}}} \mu K \left(\frac{\theta}{a_{\mathrm{e}}}\right)^2 \mathrm{d}x \tag{12}$$

and

$$U_{\mathrm{k}} = \int_0^{a_{\mathrm{e}}} \varrho I \left(\frac{\dot{a}_{\mathrm{s}}\theta}{a_{\mathrm{e}}}\right)^2 \mathrm{d}x \tag{13}$$

The external work done is

$$E = 2M_{\mathrm{s}}\theta, \tag{14}$$

the applied moment $M \equiv T(0)$ remaining at its static value

$$M_{\mathrm{s}} \equiv \mu K \left(\frac{\theta}{a_{\mathrm{e}}}\right) \tag{15}$$

Thus, from Equation 2 we have

$$P_{\mathrm{R}} = \mu K \left[2\left(\frac{\theta}{a_{\mathrm{e}}}\right)\left(\frac{\dot{\theta}}{\dot{a}_{\mathrm{s}}}\right) - \left(\frac{\theta}{a_{\mathrm{e}}}\right)^2 - \left(\frac{\varrho I}{\mu K}\right)\dot{a}_{\mathrm{s}}^2\left(\frac{\theta}{a_{\mathrm{e}}}\right)^2\right] \tag{16a}$$

or

$$P_{\mathrm{R}} = \mu K \left(\frac{\dot{\theta}}{\dot{a}_{\mathrm{s}}}\right)^2 \left[1 - \left(\frac{\dot{a}_{\mathrm{s}}}{c_{\mathrm{t}}}\right)^2\right] \tag{16b}$$

where $c_{\mathrm{t}} = (\mu K/\varrho I)^{1/2}$, which imposes an absolute upper crack speed for this deformation mode, has often been identified as the torsional wave velocity. This conclusion could be arrived at by differentiating Equation 3 and equating it to Equation 8 to form a wave equation. However, we shall later demonstrate that torsional waves may travel at up to the shear-wave velocity, and that only displacement profiles having, like Equation 7, $\phi'' = 0$ are restricted in velocity to c_{t}.

By further use of Equations 11 and 15, Equation 16 can be re-cast in a variety of forms

$$P_{\mathrm{R}}(\theta, a_{\mathrm{e}}) = \mu K \left(\frac{\theta}{a_{\mathrm{e}}}\right)^2 \left[1 - \left(\frac{\dot{a}_{\mathrm{s}}}{c_{\mathrm{t}}}\right)^2\right] \tag{16c}$$

or

$$P_{\mathrm{R}}(M_{\mathrm{s}}) = \frac{M_{\mathrm{s}}^2}{\mu K} \left[1 - \left(\frac{\dot{a}_{\mathrm{s}}}{c_{\mathrm{t}}}\right)^2\right] \tag{16d}$$

or

$$P_{\mathrm{R}}(M_{\mathrm{s}}, \theta, a_{\mathrm{e}}) = \frac{M_{\mathrm{s}}\theta}{a_{\mathrm{e}}} \left[1 - \left(\frac{\dot{a}_{\mathrm{s}}}{c_{\mathrm{t}}}\right)^2\right] \tag{16e}$$

or

$$P_{\mathrm{R}}(M_{\mathrm{s}}, \dot{\theta}, \dot{a}_{\mathrm{s}}) = \frac{M_{\mathrm{s}}\dot{\theta}}{\dot{a}} \left[1 - \left(\frac{\dot{a}_{\mathrm{s}}}{c_{\mathrm{t}}}\right)^2\right] \tag{16f}$$

amongst others in which the kinetic energy correction is similarly translated. The equivalence of these in actual use is affected not only by how near to the steady-state crack speed $\dot{a}$ is, but also on the accessibility and consistency of the other measurements.

3. Experimental method and apparatus

Two modified high density polyethylene (HDPE) pipe grades were supplied as compression-moulded 6 mm plate by BP Chemicals Limited: Rigidex 002/40, a yellow-pigmented gas pipe material, and 002/50, blue pigmented, for water pipes. Some comparative tests were also carried out on an amine-cured epoxy, Araldite MY750/HT972 (CIBA-Geigy (UK) Limited), on which extensive high-speed tests have been carried out in a parallel programme. Properties determined at very high strain rates using an ultrasonic technique* are shown in Table I. DT specimens $2H = 90$ mm wide and $L = 180$ mm long were cut from the plate, grooved 1 mm deep along one face for crack guidance, and notched with a "chevron" profile to help suppress the initiation transient. No other attempt was made to control groove or notch acuity. Since crack length and velocity must be monitored, a pattern of resistance (graphite) and conductive (silver) tracks was painted onto the grooved face, generating a double-staircase voltage-trace during fracture (Fig. 2).

Controlled crosshead displacement rates of up to 50 m sec^{-1} are impossible to maintain without extremely complicated equipment. A simpler alternative is to accelerate a sufficiently massive and well-aimed projectile, measure its velocity immediately prior to impact, and infer its subsequent deceleration from the reaction load. This was implemented using a previously-constructed vertical air gun of 1.2 m drop. The existing breech dimensions and barrel cross-section (38 mm square) imposed a size limit on the lead-ballasted steel projectile, whose 0.5 kg mass proved to be somewhat low for the slowest tests: in free-fall, the impact velocity, measured by successive interruption of two infrared beams, is about 4.5 m sec^{-1}, limiting the work input to 5 J. Under 3 bar air pressure, however (the maximum used in these tests) the projectile attains over 25 m sec^{-1} and carries over 100 J, and 20 to 30 cm depth of sand is needed to arrest it.

Two balls on the front of the impacting projectile load the specimen in four-point loading along a line 10 mm ($\equiv L-L'$) from one end. The outer support points, also spherical) are linked to a single strain gauge load cell. Output from the cell exciter/amplifier is recorded, simultaneously with that from the crack length gauge, on a Nicolet 4094 dual-channel digital oscilloscope, running in pre-trigger mode. This instrument, fitted with a twin disc drive, can both store test records permanently and carry out extensive processing on them, such as load integration and Fourier analysis.

The load measurement system, while as compact as possible, was designed to record the plateau load for

---

*The authors are indebted to Dr B. Crouch of Imperial College and Dr R. Whitehead of the Department of Materials, University of Surrey, for making these measurements.

TABLE I Properties of materials tested

Material	Temperature (°C)	Density, ϱ ($\mathrm{kg\,m^{-2}}$)	Shear Modulus, μ (GPa)	Young's Modulus, E
Rigidex 002/40	0	939	0.845	2.40
Rigidex 002/50	0	946	0.901	2.52
Araldite MY750/HT972	20	1194	1.73	4.74

fast quasi-static tests rather than the type of initiation transient which is the focus of attention in, for example, instrumented Charpy tests. It did not prove to have an extended high-frequency response but, as will be seen, provided load records whose detailed structure corresponded closely both to the crack length gauge output, and to our understanding of wave propagation effects in the specimen. Tapping the load points directly with a piezo-electric force transducer of very high resonant frequency, and comparing the two output signals and their Fourier transforms, revealed a well-damped resonance at 2.6 kHz with progressive attenuation of higher-frequency components. The load cell itself introduced an 8.3 kHz resonance which was filtered.

4. Results

All tests induced brittle crack extension. The exposed surfaces were glassy except, in HDPE, near the upper surface, where the characteristically curved DT crack front advances at a relatively low speed [7]. The upper 15 to 20% of the crack path was rough and stress-whitened; occasionally, a specimen survived testing in one piece, its two halves hinged together along this line.

4.1. Load point rotation and crack length

Some low-speed (i.e. free-fall) tests on HDPE exhibited crack arrest at an earlier stage, the projectile having bounced off. Subsequent fracture revealed a broad ($\simeq 1$ mm) stress-whitened arrest line marking the front. The majority of tests at these rates ($\dot{v} = 4.5$ to $6\,\mathrm{m\,sec^{-1}}$) did fracture the specimen completely, but the crack length record and the exposed surface both revealed a series of arrest lines. Correspondence between these was excellent, suggesting that timing track fracture generally neither preceded nor lagged material separation. This stick-slip crack growth is believed, by analogy with the phenomenon in epoxies at much lower speeds, to indicate a minimum in the material's resistance versus crack speed characteristic, corresponding to the suppression of a crack blunting mechanism. Crack velocities of less than $67\,\mathrm{m\,sec^{-1}}$ could not be observed in either material.

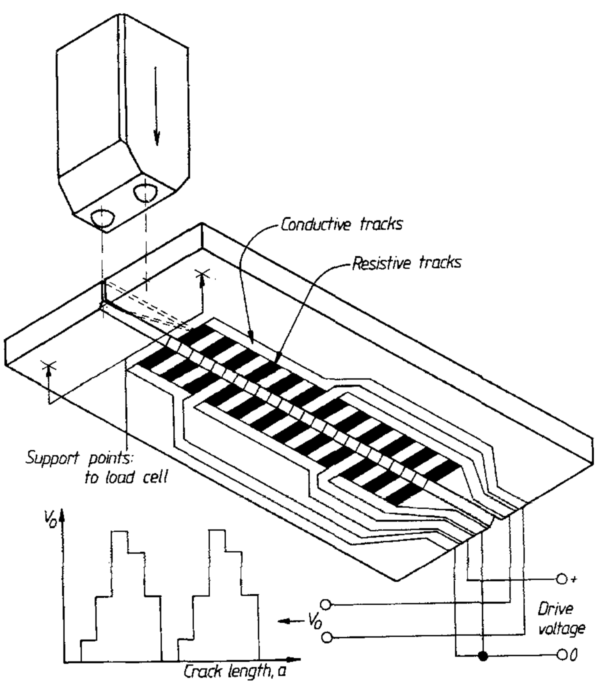

Figure 2 Drop-weight loaded DT test, showing crack length gauge.

Displacement v and displacement rate $\dot{v}$ having been computed from the load integrals, impact velocity, rotation θ and rotation rate $\dot{\theta}$ were calculated using a large-displacement analysis [9] in which the effects of rotation, impact and support point radii r_1 and r_2 and specimen thickness are accounted for. The relation

$$\frac{v}{D} = \tan\theta - \gamma(\sec\theta - 1) \qquad (17)$$

where

$$\gamma \equiv \frac{r_1 + r_2 + B}{D}$$

and D is the small-displacement moment arm, must be inverted by iteration; then

$$\dot{\theta} = \frac{\dot{v}}{D\sec^2\theta(1 - \gamma\sin\theta)} \qquad (18)$$

can be calculated directly. Rotations of up to 30°, above which the sides of the projectile hit the specimen surface, were not uncommon in HDPE. Note that even for constant $\dot{v}$ the rotation rate is not generally constant, but first accelerates and then decelerates, introducing an unaccounted for inertial element into the contact force; furthermore, the measured load must also be converted to an applied moment using the large-displacement form

$$M = \tfrac{1}{2}PD\sec^2\theta(1 - \gamma\sin\theta) \qquad (19)$$

These are the first of many difficulties in interpreting the measured load P, which we now consider in more detail.

4.2. Load against time records

DT test load traces for slow crack growth in brittle materials normally show one of two forms: an essentially linear ramp is followed by an initial drop on crack initiation ("pop-in") to either a plateau, during continuous growth, or a static re-loading ramp to subsequent re-initiation, and so on, during "stick-slip" crack growth. Tests on HDPE provided similar

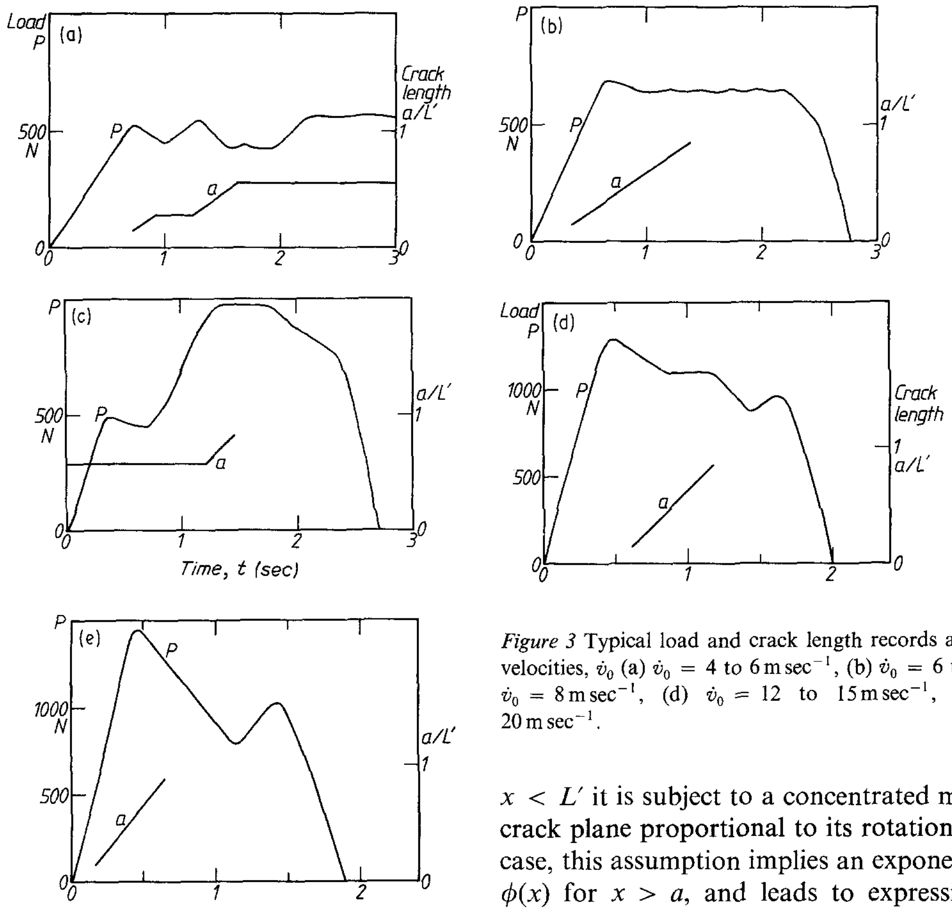

Figure 3 Typical load and crack length records at various impact velocities, $\dot{v}_0$ (a) $\dot{v}_0 = 4$ to $6\,\mathrm{m\,sec^{-1}}$, (b) $\dot{v}_0 = 6$ to $12\,\mathrm{m\,sec^{-1}}$, (c) $\dot{v}_0 = 8\,\mathrm{m\,sec^{-1}}$, (d) $\dot{v}_0 = 12$ to $15\,\mathrm{m\,sec^{-1}}$, (e) $\dot{v}_0 = 15$ to $20\,\mathrm{m\,sec^{-1}}$.

P/t records: stick-slip up to about $6\,\mathrm{m\,sec^{-1}}$ (Fig. 3a) and continuous growth at higher rates (Fig. 3b). When corrected for delay due to the load linkage (0.1 m sec) and to torsional wave propagation at the shear wave velocity $c_s \equiv (\mu/\varrho)^{1/2}$, the load drops corresponded closely to recorded crack jumps.

Virtually all tests showed periods of constant-velocity crack growth covering at least 30 to 40 mm – sometimes 100 mm. As the crack approached the end $a = L'$, it generally decelerated slightly (in contrast to typical behaviour in slow-rate tests), but extrapolation from the last track at $a = 140$ mm still suggested load to be sustained for long after end breakthrough at $L' = 170$ mm. This illustrates the low-rate ductility of HDPE; considerable work is absorbed by the hinge on the upper specimen surface, although this work is not, as in some Charpy test analyses, included in the resulting toughness measurement.

For impact velocities exceeding $12\,\mathrm{m\,sec^{-1}}$, the resemblance to quasi-static load/time records fades rapidly. It becomes clear that considerable crack growth has occurred before a load drop is registered, while most of the plateau region is attributable to ductile hinging. While much information above 2.6 kHz in the applied load signal has been lost, we consistently observe that remaining details can be explained in terms of axial wave propagation phenomena, which are now considered in some detail.

The beam root model [8], mentioned above in connection with root compliance prediction, assumes each half of the specimen to behave as an independent torsion beam (i.e. any section rotating and warping only) along its entire length L, although for $a < x < L'$ it is subject to a concentrated moment at the crack plane proportional to its rotation. In the static case, this assumption implies an exponential decay in $\phi(x)$ for $x > a$, and leads to expressions for root compliance and crack shape. In the dynamic case, it can be shown [10] that waves of sufficiently high frequency will travel indefinitely along such a supported beam. As seen from the load plane, the beam root is therefore quite rigid and reflective (as assumed in a previous dynamic DT analysis [11]) to low frequency energy, but it is compliant and transparent to high frequency waves. These are subsequently reflected off the end face with an inversion, and pass back through the beam root to be recorded at the load plane. It is shown in Appendix A that high-frequency torsional waves travel at approximately the shear wave velocity.

Return of the inverted impact wavefront after a period $2L'/c_s$ was easily observable on most P/t records, but is best illustrated by one in which a long initial crack (from the arrested low-rate test of Fig. 3a) was reloaded at higher speed (Fig. 3c). The successive low-frequency wave reflections of Popelar's model [11] which settle into quasi-static torsion of the free beam in $0 < x < a$ are hardly detectable, but the reflected high-frequency wave packet arrives at exactly the expected time, unloading the plane $x = 0$ long before crack re-initiation. After a further period $2L'/c_s$, unloading abruptly ceases as the wavefront which it has itself propagated returns to assist loading. Further reflections are rarely observable since continuing end torsion θ/a_e grows to dominate smaller torsions due to wave propagation, and because the supported beam in $a < x < L'$ disperses wave energy by transmitting longer wavelengths slower than shorter ones [10]. Note that the characteristic frequency of this deformation mode is less than 1.5 kHz, well below the minimum resonance of the load measurement system; load pulses, generated as described above, are passed without significant distortion at this time-scale.

Crack initiation, which sends an unloading wave backwards and a loading wave forwards, further complicates the picture. It was observed that initiation of a slow crack influenced the load trace almost immediately, whereas initiation of a fast crack influenced it significantly only after a period corresponding to end reflection and inversion of the forward loading wave. This is essentially a Doppler effect whereby, with increasing crack speed, an upward shift in the frequency of the forward wave, enabling its transmission through the beam root, is balanced by a reduction in the rearward unloading rate. Load/time traces for high speed tests present a strange picture, in which crack initiation and propagation hardly seem to unload the specimen. The load continues to rise rapidly until the arrival of the inverted impact wave, closely followed or simultaneous with the arrival of the inverted initiation wave, starts to reverse it (Fig. 3e).

In summary, although the bandwidth of the load-cell based recording system used was limited, significant features of the load/time signal which arose from wave propagation phenomena lay well within it. These phenomena may in themselves, however, make the measured load at any time unrepresentative of the crack tip environment.

5. Discussion

These observations narrow the choice of methods for calculating R. The load-point moment M is a poor indicator of the work input to the near-tip region (particularly at high impact speeds) where Fig. 4 shows that the load sampled at moderate crack lengths far exceeded the quasi-static value computed from Equation 15. At lower speeds, many tests yielded loads lower than this prediction, probably due to projectile deceleration. The crucial issue is to what extent these disparities are reflected on the near-tip energy balance. Although the quasi-static moment value (Equation 15) is implicit in all of Equations 16, its explicit appearance in variants D, E and F is associated with unacceptable scatter on the R values calculated from them (not plotted) and we are justified in rejecting them.

R values were also computed by Methods B and C, and the latter are plotted in Fig. 5. These show no more scatter than other dynamic test methods, and indicate a clear, near-constant minimum of $2\,\mathrm{kJ\,m^{-2}}$ ($K_{\mathrm{IC}} = 2.2\,\mathrm{MPam^{1/2}}$) with little distinction between the two materials. The results from Method B, however, show no relationship between R and $\dot{a}$ at all and are not plotted. Since they are a factor of $(\dot{a}/\dot{a}_s)^2$ larger than those plotted in Fig. 5, the problem is illustrated by Fig. 6: although DT cracks tend to run at a constant velocity, any bias towards the "steady-state" value is rather weak. They generally run slower, but the overall indeterminancy is particularly severe in the $\dot{a}$ = 120 to $150\,\mathrm{m\,sec^{-1}}$ range, where some run very much faster. It is interesting to note that this is the range of crack velocities within which Fig. 5 suggests that R may fall with increasing $\dot{a}$, an inherently unstable characteristic. Fracture surfaces here show clear arrest lines, so that stick-slip crack propagation certainly occurred, although it may only have been precipitated by torsion wave interactions.

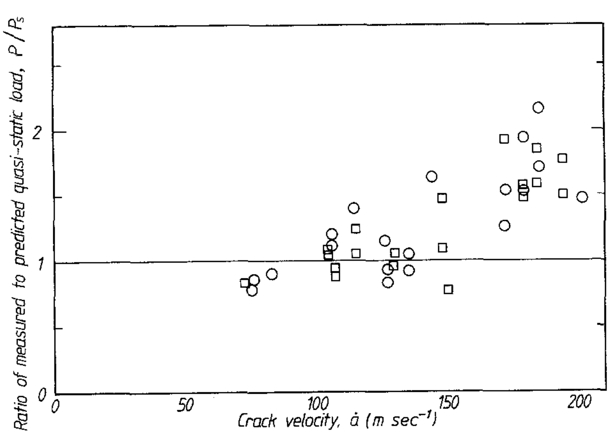

Figure 4 Comparison of measured load during fracture with that predicted quasi-statically from displacement and crack length. (○) Rigidex 002/40, (□) Rigidex 002/50.

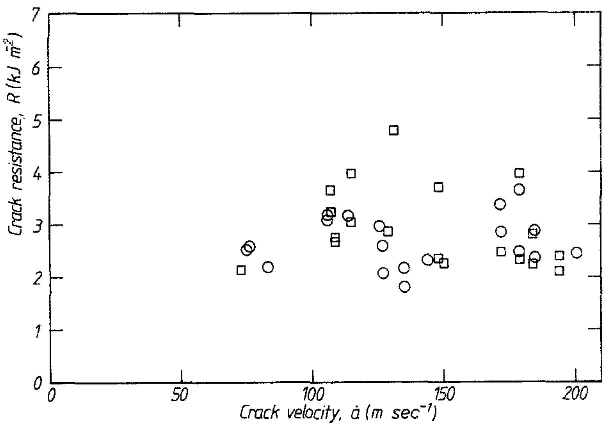

Figure 5 Crack resistance as a function of crack velocity. Computed by quasi-static analysis from displacement and crack length data. (○) Rigidex 002/40, (□) Rigidex 002/50.

6. Further analysis: dynamic effects

Because θ and a_e clearly constitute a satisfactory first-order description of the specimen deformation, the consistency in R values computed from it is unlikely to be merely fortuitous. However, the conditions on which the quasi-static analysis rest are not exactly met, and second-order terms involving inertial effects should be accounted for if greater accuracy is to be sought. The essentially one-dimensional nature of the DT specimen greatly facilitates an "assumed displacement" analysis, in which an evolving non-linear

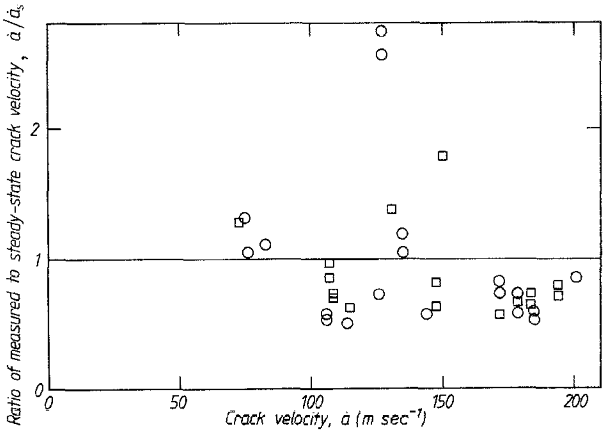

Figure 6 Comparison of measured crack velocity with steady-state value. (○) Rigidex 002/40, (□) Rigidex 002/50.

rotation profile $\phi(x)$ is sought which satisfies specified boundary conditions, but along which inertial forces arise and are (at least at some points) in equilibrium. To illustrate the approach, we consider a cubic profile satisfying steady-state boundary conditions:

(a) constant rotation rate, $\ddot{\theta} = 0$;
(b) constant crack speed, $\ddot{a} = 0$;
(c) near-tip rotation constant and equal to the quasi-static value

$$\phi(a) = (a - a_e)\frac{\partial \phi}{\partial x}(a) \qquad (20)$$

and, most critically,
(d) quasi-static conditions in the beam support $x > a$. This is implemented as

$$\frac{\partial^2 \phi}{\partial x \partial a} = 0 \qquad (21)$$

The last condition is based on the idea that P_R remains, like $\dot{a}$, constant, and could be computed by any of Equations 16 by replacing θ by $\phi(a)$, a_e by $(a_e - a)$ and M_s by $T(a)$; to derive Equation 21, we choose Equation 16c. However, Appendix A shows that for non-linear $\phi(x)$ profiles, Equation 3 must be modified to

$$T = -\mu K \phi' \left[1 + F\left(\frac{H\phi''}{\phi'}\right)^2\right] \qquad (22)$$

where $' = \partial/\partial x$, etc, and

$$F = \tfrac{1}{24}(1 + \nu) \qquad (23)$$

so that if ϕ'' exists at $x = a$, torque can be transmitted through the crack tip at a lower ϕ'. We account for this fact by calculating P_R through an energy balance as

$$P_R = T(a)\frac{\dot{\phi}(a)}{a} - \varrho I \dot{\phi}^2(a) \qquad (24)$$

that is, not putting $T(a) = \mu K \phi(a)/a$; however, we do not account for it in Equation 21 since this renders analysis almost intractable. The effect is to overestimate the kinetic correction and thus to underestimate P_R.

The rotation profile

$$\phi(x, a) = \theta + A_1(a)x + A_2(a)x^3 \qquad (25)$$

automatically satisfies equilibrium at $x = 0$, since $\phi''(0) = 0$. To satisfy Equation 20, we find that

$$A_1 = a^2 A_2\left(2\frac{a}{a_e} - 3\right) - \frac{\theta}{a_e} \qquad (26)$$

and to satisfy Equation 21 that

$$\phi'(a) = A_1 + 3a^2 A_2 = q \qquad (27)$$

q being a constant. The required profile becomes

$$\phi(x) = \theta + \left(1 - \frac{3}{2}\frac{a_e}{a}\right)qx - \frac{3}{2}\theta\frac{x}{a} + \tfrac{1}{2}(\theta + qa_e)\left(\frac{x}{a}\right)^3 \qquad (28)$$

from which q can be determined by satisfying equilibrium for the beam as a whole. At any section, the rotation rate is ($\ddot{a} = 0$)

$$\begin{aligned}\dot{\phi} &= \left[\frac{\partial \phi}{\partial \theta}\frac{\dot{\theta}}{\dot{a}} + \frac{\partial \phi}{\partial a_e} + \frac{\partial \phi}{\partial a}\right]\dot{a} \\ &= \left[1 - \frac{3}{2}\left(\frac{x}{a}\right) + \frac{1}{2}\left(\frac{x}{a}\right)^3\right]\dot{\theta} \\ &\quad + \frac{3}{2}\left\{\left[\left(\frac{a_e}{a} - 1\right)q + \frac{\theta}{a}\right]\frac{x}{a} \right. \\ &\quad \left. - \left[\left(\frac{a_e}{a} - \frac{1}{3}\right)q + \frac{\theta}{a}\right]\left(\frac{x}{a}\right)^3\right\}\dot{a} \qquad (29)\end{aligned}$$

and the angular acceleration is ($\ddot{\theta} = 0$)

$$\begin{aligned}\ddot{\phi} &= \left[2\frac{\partial^2 \phi}{\partial \theta \partial a}\frac{\dot{\theta}}{\dot{a}} + 2\frac{\partial^2 \phi}{\partial a \partial a_e} + \frac{\partial^2 \phi}{\partial a^2}\right]\dot{a}^2 \\ &= 3\frac{\dot{a}^2}{a}\left\{\left[q\left(1 - \frac{a_e}{a}\right) - \frac{\theta}{a} + \frac{\dot{\theta}}{\dot{a}}\right]\left(\frac{x}{a}\right) \right. \\ &\quad \left. - \left[q\left(1 - 2\frac{a_e}{a}\right) - 2\frac{\theta}{a} + \frac{\dot{\theta}}{\dot{a}}\right]\left(\frac{x}{a}\right)^3\right\} \qquad (30)\end{aligned}$$

The inertial moment for the beam $0 < x < a$ is

$$\begin{aligned}M_I &= \varrho I \int_0^a \ddot{\phi}\, dx \\ &= \tfrac{3}{4}\varrho I \dot{a}^2\left[q + \frac{\dot{\theta}}{\dot{a}}\right] \qquad (31)\end{aligned}$$

Now, from Equation 22 we find that the applied moments at the beam ends must be

$$M \equiv T(0) = -\mu K\left[\left(1 - \frac{3a_e}{2a}\right)q - \frac{3}{2a}\right] \qquad (32)$$

and

$$T(a) = -\mu K\left[q + \frac{9F}{q}\left(\frac{H}{a}\right)^2\left(\frac{\theta}{a} + q\frac{a_e}{a}\right)\right] \qquad (33)$$

so that the equilibrium condition

$$M_I = M - T(a)$$

reduces to the quadratic in q:

$$\begin{aligned}&\left[1 - \frac{1}{2}\left(\frac{\dot{a}}{c_t}\right)^2\frac{a}{a_e} + 6F\left(\frac{H}{a}\right)^2\frac{a_e}{a}\right]q^2 \\ &+ \frac{\theta}{a_e}\left[1 - \frac{1}{2}\left(\frac{\dot{a}}{c_t}\right)^2\frac{\dot{a}_s}{a}\frac{a}{a_e} + 12F\left(\frac{H}{a}\right)^2\frac{a_e}{a}\right]q \\ &+ \left(\frac{\theta}{a}\right)6F\left(\frac{H}{a}\right)^2\frac{a_e}{a} = 0 \qquad (34)\end{aligned}$$

whose solution is straightforward given all of the geometric parameters.

Since $\dot{\phi}(a) = -q\dot{a}$ and $T(a)$ is given by Equation 33, Equation 24 becomes

$$\begin{aligned}P_R = \mu K q^2 &\left[1 - \left(\frac{\dot{a}}{c_t}\right)^2 \right. \\ &\left. + 9F\left(\frac{H}{a}\right)^2\left(\frac{a_e}{a}\right)^2\left(1 + \frac{1}{q}\frac{\theta}{a_e}\right)^2\right] \qquad (35)\end{aligned}$$

The existence of the last term in Equation 35 shows that energy supply to the crack tip can be maintained for $\dot{a} > c_t$.

If the stiffening effect of beam curvature could be neglected, Equation 34 would reduce to

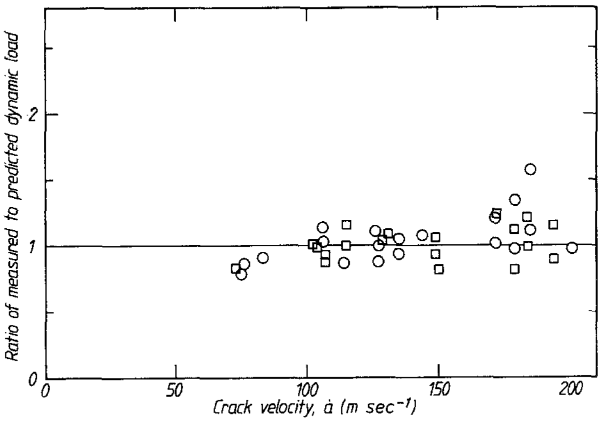

Figure 7 Comparison of measured load during fracture with that corresponding to one of two displacement modes allowed by the dynamic analysis. (○) Rigidex 002/40, (□) Rigidex 002/50.

$$q = \frac{\theta}{a_e}\left[\frac{1 - \frac{1}{2}(\dot{a}_s/\dot{a})(\dot{a}/c_t)^2}{1 - \frac{1}{2}(\dot{a}/c_t)^2}\right] \tag{36}$$

whence

$$M = \frac{\theta}{a_e}\left[\frac{1 - \frac{1}{2}(\dot{a}/c_t)^2(\frac{3}{2} - \frac{1}{2}(\dot{a}_s/\dot{a}))}{1 - \frac{1}{2}(\dot{a}/c_t)^2}\right] \tag{37}$$

and

$$P_R = \frac{1}{\mu K}\left(\frac{\theta}{a_e}\right)^2\left[\frac{1 - \frac{1}{2}(\dot{a}_s/\dot{a})(\dot{a}/c_t)^2}{1 - \frac{1}{2}(\dot{a}/c_t)^2}\right]^2 \times \left[1 - \left(\frac{\dot{a}}{c_t}\right)^2\right] \tag{38}$$

For each test, P_R and P (from Equations 32 and 19) were calculated for each of the two roots q, representing different admissible deformation modes. One root was always very close to this low-curvature solution and produced R values quite close to those of Equation 16c plotted in Fig. 5, although the corresponding loads were often very different. The other root was associated with a greater near-tip ϕ'' value, and yielded a higher load value and at low crack velocities a lower R value. At higher velocities, this second root produced a higher R value. In each case, it was easy to establish which mode operated by comparing the predicted load with that actually measured; Fig. 7 shows that for the selected mode agreement was much better than for the quasi-static value (Fig. 4).

R values for HDPE calculated by this analysis are plotted in Fig. 8. They closely resemble those computed using the quasi-static analysis using θ/a_e (Equation 16c), and, since they are based to some degree on all of the known boundary conditions, lend them additional support. It is believed that the lower R values yielded by this approximate dynamic analysis are mainly due to shortcomings already discussed, so that the more easily derived quasi-static results may well be of at least equivalent accuracy.

It is interesting to consider briefly the results of tests on Araldite MY750 in this context. The higher modulus and lower toughness resulted in very high crack velocities (up to 400 m sec^{-1}) for quite modest impact velocities, but these still always fell short of $\dot{a}_s$. For these specimens, c_t was 300 m sec^{-1}, confirming our hypothesis that it does not impose a limiting velocity on non-linear torsion profiles, and suggesting that far higher velocities can be achieved in HDPE than those so far attained – some recent tests have fulfilled this. Here, the quasi-state analysis fails, producing negative R values. For Araldite, large volumes of data, computed by finite-element analysis of single edge notch and double cantilever beam specimens [12] fracturing under constant displacement, have still left some doubts about the underlying $R(\dot{a})$ characteristic (assuming its unique existence). From a low-velocity plateau, this appears to sweep up to very high values at a geometry-dependent limiting velocity of 300 to 330 m sec^{-1}. DT results using our dynamic analysis, however, produce high-velocity R values lower than the plateau, and, at the highest velocity, negative. Clearly, further development is necessary to avoid an inherent tendency to under-estimate R, and will provide a considerably more valuable test.

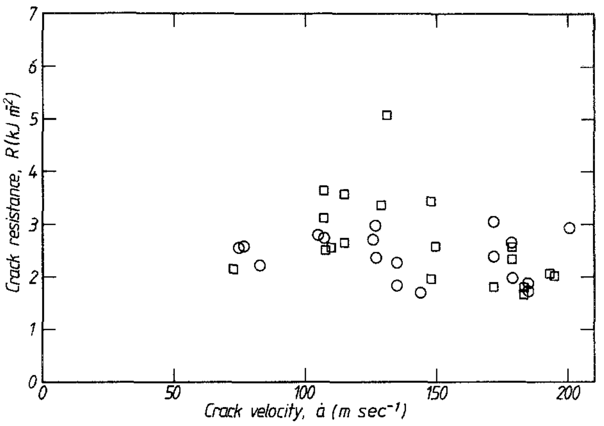

Figure 8 Crack resistance as a function of crack velocity in two HDPE grades. Computed by dynamic analysis from displacement, displacement rate, crack length and velocity data. (○) Rigidex 002/40, (□) Rigidex 002/50.

Finally, we note the relevance of recent lumped-parameter analysis of the Charpy impact test [15]. Embracing contact stiffness effects by extension from a mass-spring-support to a spring-mass-spring-support model introduces wave-like behaviour, although waveguide-like behaviour of the specimen itself is not considered. Due to the spectrum of possible vibrational modes, even if the material has a constant-R characteristic, quasi-statically computed values using displacement data only can scatter around it by discrete factors which multiply and diverge as the time-scale falls. An apparent R characteristic emerges whose average value and scatter increase rapidly with $\dot{a}$ as an artificial limiting velocity is approached. This is such a common picture in data from materials, such as Araldite, whose fractography and dynamic properties would not in themselves lead one to expect strong rate dependence in R, that similar effects might be suspected to be occurring in other geometries. The DT geometry is, of course, waveguide-like without considering contact stiffness. Our dynamic model effectively discretises it by restricting its torsion profile $\phi(x)$ to a reduced cubic, and satisfying equilibrium only at one point. A second R value emerges because of the curvature-dependent torque/torsion relation – but here we are able to discriminate between them using a parameter (load) redundant to the quasi-static analysis. It is, therefore, to be hoped that considering higher-order terms in $\phi(x)$ in further development of the analysis may help to reduce scatter further, if sufficiently accurate load measurements can be used to discriminate more finely between deformation modes.

7. Conclusions

Brittle fracture can be induced repeatably in small specimens of highly ductile gas and water pipe grade polyethylenes, using a simple drop-weight loaded double torsion (DT) specimen. Crack resistance, R, during steady high-speed crack propagation can be estimated reliably, from crack length and projectile displacement data, using a simple quasi-static deformation analysis. However, crack propagation can be sustained at well above the conventionally-defined torsional wave speed, yielding negative R values by this method; these high velocities are explained by the ability of torsional waves of non-uniform twist to travel at up to the higher shear wave speed. An estimate of the torque/twist relation for this generalized situation leads to an approximate dynamic analysis which supports the quasi-static results at low crack velocities while yielding finite (though somewhat low) results for high velocities. The model is capable of considerable refinement without modifying the underlying hypotheses.

Appendix A

Non-uniform torsion of a rectangular beam

Consider the elemental length of a rectangular-sectioned torsion beam shown in Fig. A1. The displacement system

$$\begin{aligned} v_x &= \psi(y, z)\phi' \\ v_y &= -\phi z - v \int \psi\phi'' \, dy \qquad \text{(A1)} \\ v_z &= \phi y - v \int \psi\phi'' \, dz \end{aligned}$$

accounts for a small rotation ϕ due to torsion, for warping $\psi(y, z)$ and, through the integral terms, for unconstrained in-plane contraction under axial stress (a realistic assumption for small ϕ''). Equations A1 imply strains

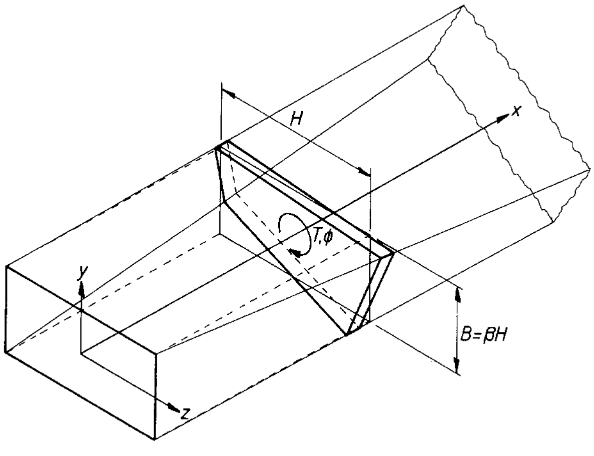

Figure A1 Rectangular beam under torsion

$$\begin{aligned} e_{xx} &= \psi(y, z)\phi'' \\ e_{yy} &= e_{zz} = -v e_{xx} \\ e_{xy} &= \left(\frac{\partial\psi}{\partial y} - z\right)\phi' - v\frac{\partial}{\partial x}\int \psi\phi'' \, dy \qquad \text{(A2)} \\ e_{xz} &= \left(\frac{\partial\psi}{\partial z} + y\right)\phi' - v\frac{\partial}{\partial x}\int \psi\phi'' \, dz \end{aligned}$$

and

$$e_{yz} = -v\phi''\left[\frac{\partial}{\partial z}\int \psi \, dy + \frac{\partial}{\partial y}\int \psi \, dz\right]$$

The strain energy density is

$$\mu\left[\tfrac{1}{2}(e_{xy}^2 + e_{xz}^2 + e_{yz}^2) + (e_{xx}^2 + e_{yy}^2 + e_{zz}^2) + \frac{v}{1 - 2v}(e_{xx} + e_{yy} + e_{zz})^2\right] \qquad \text{(A3)}$$

To achieve a first-order estimate of the effects of ϕ derivatives, we neglect not only terms in ϕ''', but also those arising from in-plane shear. The strain energy per unit length becomes

$$u_e = \mu\phi'^2 \int_{-H/2}^{H/2}\int_{-B/2}^{B/2}\left\{\frac{1}{2}\left[\left(\frac{\partial\psi}{\partial y} - z\right)^2 + \left(\frac{\partial\psi}{\partial z} - y\right)^2\right] + (1 + v)\left(\frac{\phi''}{\phi'}\right)^2\psi^2\right\} dy \, dz \qquad \text{(A4)}$$

The warping function ψ must satisfy Laplace's equation and stress-free boundary conditions; the exact solution is an antisymmetric infinite series [13]. The lowest-order non-trivial approximation is a cubic which can be expressed as

$$\psi = yz[1 - 2m\beta + n\beta(y^2 - z^2)/H^2] \qquad \text{(A5)}$$

where $\beta \equiv B/H$, whence

$$\begin{aligned} u_e = \tfrac{1}{6}\mu B^3 H\phi'^2\{&m^2 + (1 - m\beta)^2 \\ &+ \tfrac{3}{20}n[m(1 - \beta^4) - \tfrac{5}{3}\beta + \beta^3] + \tfrac{3}{16}n^2[\tfrac{1}{28} + g_1] \\ &+ \tau[(1 - 2m\beta)^2 - \tfrac{3}{10}n\beta(1 - 2m\beta)(1 - \beta^2) \\ &+ \tfrac{3}{16}n^2\beta^2 g_2]\} \end{aligned} \qquad \text{(A6)}$$

where

$$\begin{aligned} g_1 &\equiv \beta^2[\tfrac{1}{20}(1 + \beta^2) + \tfrac{1}{28}\beta^4] \\ g_2 &\equiv \beta^2[\tfrac{1}{7} - \tfrac{6}{25}\beta^2 + \tfrac{1}{7}\beta^4] \end{aligned}$$

and

$$\tau \equiv \frac{(1 + v)}{24}\left(\frac{H\phi''}{\phi'}\right)^2$$

Equilibrium can now be satisfied approximately by determining m and n values which yield a minimum in u. This procedure yields

$$m = \beta\left\{\frac{(\frac{1}{28} + g_1 + \tau\beta^2 g_2)(1 + 2\tau) - \frac{3}{100}(1 - \beta^2)(1 + \beta^2[1 + 4\tau])[\frac{2}{3} + (1 - \beta^2)(1 + 2\tau)]}{[(\frac{1}{28} + g_1 + \tau\beta^2 g_2) - \frac{3}{100}(1 - \beta^2)^2(1 + \beta^2[1 + 4\tau])][1 + \beta^2(1 + 4\tau)]}\right\} \quad \text{(A7)}$$

and

$$n = -\frac{2}{5}\left\{\frac{(1 - \beta^2)(m[1 + \beta^2(1 + 4\tau)] - \beta[1 + 2\tau]) - \frac{2}{3}\beta}{(1 - \beta^2)[1 + \beta^2(1 + 4\tau)]}\right\} \quad \text{(A8)}$$

whose successive solution and substitution into Equation A6 solves for

$$u_e = \tfrac{1}{6}\mu B^3 H\phi'^2 u^*(\beta, \tau) \quad \text{(A9)}$$

For a process of torsion only, and in which inertial forces are absent or do not significantly modify deformations and kinetic energy of torsion and warping is negligible, the external work done is $-\frac{1}{2}T\phi'$ per unit length and an energy balance leads to

$$T = -\mu(\tfrac{1}{3}HB^3)u^*(\beta, \tau)\phi' \quad \text{(A10)}$$

The exact solution for $\tau = 0$ is

$$T = -\mu ZHB^3\phi'$$

where $Z(\beta)$ is a tabulated function [13] which is compared with $\frac{1}{3}u^*(\beta, 0)$ in Table AI. Although higher terms are needed to accommodate boundary conditions for low but finite β, the cubic approximation is close enough to justify writing the non-uniform torsion equation as

$$T = -\mu K\phi' T^*(\beta, \tau) \quad \text{(A11)}$$

where

$$T^* \equiv \frac{u^*(\beta, \tau)}{u^*(\beta, 0)}$$

and μK is the exact polar torsional rigidity.

Computed values of $T^*(\beta, \tau)$ are plotted in Fig. A2. For very thin beams

$$T(0, \tau) = -\mu K\phi'[1 + \tfrac{1}{24}(1 + \nu)(1 + (\phi''/\phi')^2)] \quad \text{(A12)}$$

and this remains an acceptable correction up to $\beta \simeq 0.2$ and $\tau \simeq 0.5$. For higher β (squarer sections) the greater polar symmetry reduces non-uniform torsion stiffening; a round bar, for which no warping occurs, will of course exhibit none.

For a process of torsion and rotation of the element in which rotational kinetic energy is significant, rotational equilibrium in the absence of external moments requires that

$$\frac{\mathrm{d}T}{\mathrm{d}x} + \varrho I\ddot{\phi} = 0 \quad \text{(A13)}$$

TABLE AI The torsion constant $u^*(\beta, 0)$ from this analysis compared to the exact value tabulated in [13]

$H/B = \beta^{-1}$	$\frac{1}{3}u^*(\beta, 0)$	$Z(\beta)$
1.0	0.1407	0.1406
1.2	0.166	0.166
1.5	0.196	0.196
2.0	0.231	0.229
2.5	0.253	0.249
3.0	0.268	0.263
4.0	0.288	0.281
5.0	0.301	0.291
10.0	0.323	0.312
∞	0.333	0.333

which, using Equation A11, becomes a non-linear wave equation:

$$\ddot{\phi} - c_t^2\phi''\left[T^* - 2\tau\frac{\mathrm{d}T^*}{\mathrm{d}\tau}\left(1 - \frac{\phi'\phi'''}{\phi''^2}\right)\right] = 0 \quad \text{(A14)}$$

where $c_t^2 \equiv \mu K/\varrho I$. For small β, this reduces to

$$\ddot{\phi} - c_t^2\phi''\left\{1 + \frac{(1 + \nu)}{24}H^2\left[2\frac{\phi'''}{\phi'} - \left(\frac{\phi''}{\phi'}\right)^2\right]\right\} = 0 \quad \text{(A15)}$$

which, even in the simplest case, has no constant-amplitude, finite-wavelength harmonic solutions. The anomalous singular behaviour of Equation A15 at extrema in ϕ is largely due to the neglect of ϕ''' terms in Equation A2, but the cases analysed in Appendix B and the text are not seriously affected.

Consider now large-τ rotation profiles: those of large amplitude or small wavelength. Fig. A2 already suggests that as $\tau \to \infty$ for $\beta > 0$, T^* approaches a limit, and inspection of Equations A6 to A8 shows that

$$u^*(\beta, \infty) = \frac{(1 + \beta^2)}{4\beta^2} \quad \text{(A16)}$$

This corresponds to complete suppression of warping, so that the assumptions made to derive the approximate small-τ solution (no in-plane shear contribution to strain energy, no inertial constraints on warping)

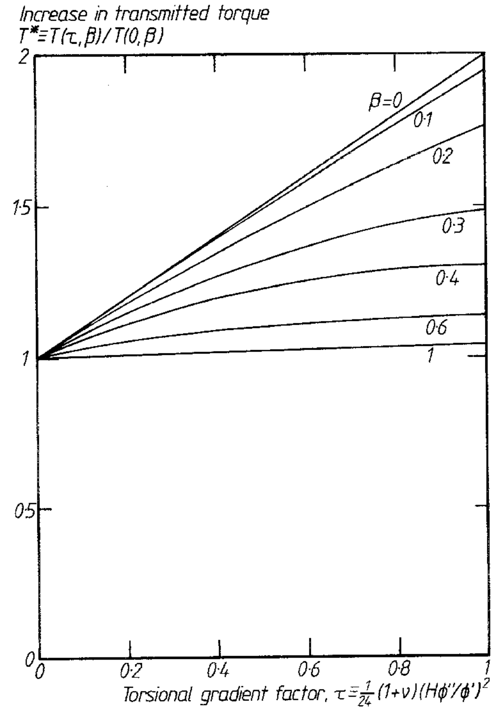

Figure A2 Stiffening effect of non-uniform torsion in a rectangular beam.

lose their importance. Since $\mathrm{d}u^*/\mathrm{d}\tau \rightarrow 0$, the wave equation regains linearity:

$$\ddot{\phi} - c_s^2 \phi'' = 0 \tag{A17}$$

where $c_s \equiv (\mu/\varrho)^{1/2}$ is the material shear wave velocity, and constitutes the limiting speed of torsional waves in beams of any section.

Appendix B

Torsion of a rectangular beam in which one section remains plane

This situation has been analysed by Timoshenko [14] using an approximate method analogous to that of Appendix A, and therefore provides a suitable test case.

A thin ($\beta \rightarrow 0$) rectangular beam of length $-L < x < L$ is prevented from rotating at mid-span, and subjected to equal moments M at its ends. The static torque at any section is

$$\begin{aligned} T &= M \quad , \quad -L < x < 0 \\ T &= -M \quad , \quad 0 < x < L \end{aligned} \tag{B1}$$

Clearly, $\phi'(x)$ and its associated warping function ψ are symmetrical in x, and the latter, being antisymmetrical in (y, z), is zero at $x = 0$. Let the beam be cut at this section. The torque distribution remains identical, but the separated faces are now free to warp incompatibly, with axial displacements $\pm v_x(y, z)$. Timoshenko reasoned that compatibility was previously maintained by tensile stresses $p_{xx}(y, z)$ proportional to the gap left by their removal, and, assuming these to decay exponentially with $\pm x$, showed that their removal caused the end rotation to increase form θ to θ_0, where

$$\frac{\theta}{\theta_0} = 1 - \frac{[5(1 + \nu)]^{1/2}}{6} \frac{H}{L} \tag{B2}$$

The present analysis differs in regarding $\phi(x)$ as prescribed. The local torque is

$$\begin{aligned} T(x) &= -\mu\kappa\phi' \left[1 + \tfrac{1}{24}(1 + \nu) \left(\frac{H\phi''}{\phi'} \right)^2 \right] \\ &= M \end{aligned}$$

and, clearly, in the unconstrained case,

$$M = -\mu K \frac{\theta_0}{L}$$

Thus, defining $\phi^* \equiv \phi/\theta$, $x^* \equiv x/L$, $\phi^{*\prime} \equiv \mathrm{d}\phi^*/\mathrm{d}x^*$, etc., we have

$$\phi^{*\prime} \left[1 + \tau^* \left(\frac{\phi^{*\prime\prime}}{\phi^{*\prime}} \right)^2 \right] - 1 = 0 \tag{B3}$$

which can easily be solved from $\phi^{*\prime} = 0$ at $x^* = 0$ using a finite difference formulation for any value of the parameter

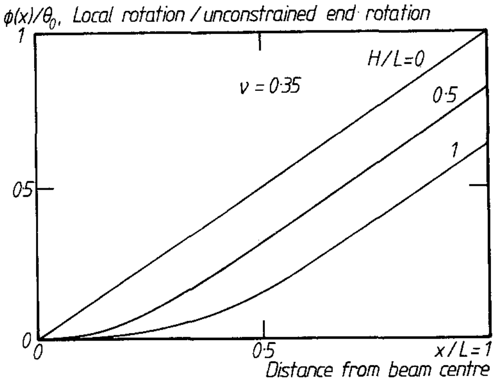

Figure B1 Rotation profiles of a thin rectangular beam, $2L$ long, held at its centre and twisted at both ends.

$$\tau^* \equiv \tfrac{1}{24}(1 + \nu) \left(\frac{H}{L} \right)^2 \tag{B4}$$

Typical rotation profiles for various (H/L) ratios with $\nu = 0.35$ are plotted in Fig. B1. Because the region of non-uniform torsion is so localised, θ/θ_0 falls linearly with (H/L) for $H < L$, and the result can be expressed as

$$\frac{\theta}{\theta_0} = 1 - 0.315(1 + \nu)^{1/2} \left(\frac{H}{L} \right) \tag{B5}$$

The numerical factor is some 15% less than that due to Timoshenko.

References

1. A. GRAY, J. N. MALLINSON and J. B. PRICE, *Plastics & Rubber: Processing & Applications* **1** (1981) 51.
2. J. M. GREIG and L. EWING, "Fracture Propagation in Polyethylene (PE) Gas Pipes", in "Plastics Pipes V", York, UK, 8–10 September (PRI, London, 1982).
3. R. W. E. SHANNON and A. A. WELLS, *Int. J. Fracture* **10** (1974) 471.
4. W. A. MAXEY, "Fracture Initiation, Propagation and Arrest", AGA 5th Symposium on Line Pipe Research (1974).
5. R. VAN CROMBRUGGE, "Fracture Propagation in Plastic Pipe", in "Plastics Pipe V", York, UK, 8–10 September (PRI, London, 1982).
6. P. KRISHASWAMY, private communication 1984.
7. P. S. LEEVERS, *J. Mater. Sci.* **17** (1982) 2469.
8. P. S. LEEVERS and J. G. WILLIAMS, *ibid.* **20** (1985) 77.
9. P. S. LEEVERS, *J. Mater. Sci. Lett.* **5** (1986) 191.
10. C. A. COULSON and A. JEFFREY, "Waves" 2nd edn (Longman, London, 1977).
11. C. H. POPELAR, "Crack Arrest Methodology and Applications", ASTM STP 711, edited by G. T. Hahn and M. F. Kanninen, (ASTM, Philadelphia, 1980) p. 24–37.
12. B. A. CROUCH, PhD thesis, University of London (1986).
13. S. P. TIMOSHENKO, and J. N. GOODIER, "Theory of Elasticity", 3rd edn, (McGraw-Hill, New York, 1970).
14. S. P. TIMOSHENKO, *Proc. London Math. Soc.* 2nd series, **20** (1922) 389.
15. J. G. WILLIAMS, "The Analysis of Dynamic Fracture Using Lumped Mass-Spring Models", submitted to *Int. J. Fracture*.

Received 8 May
and accepted 23 July 1986